

CHEMICAL PHYSICS

Crystal nucleation in metallic alloys using x-ray radiography and machine learning

Enzo Liotti,^{1*} Carlos Arteta,² Andrew Zisserman,² Andrew Lui,¹ Victor Lempitsky,³ Patrick S. Grant¹

The crystallization of solidifying Al-Cu alloys over a wide range of conditions was studied *in situ* by synchrotron x-ray radiography, and the data were analyzed using a computer vision algorithm trained using machine learning. The effect of cooling rate and solute concentration on nucleation undercooling, crystal formation rate, and crystal growth rate was measured automatically for thousands of separate crystals, which was impossible to achieve manually. Nucleation undercooling distributions confirmed the efficiency of extrinsic grain refiners and gave support to the widely assumed free growth model of heterogeneous nucleation. We show that crystallization occurred in temporal and spatial bursts associated with a solute-suppressed nucleation zone.

INTRODUCTION

During cooling of a liquid metallic alloy, solidification proceeds first by the nucleation of solid crystals, normally at or close to the melting temperature of the alloy, and second by the growth of these crystals as the latent heat of fusion is removed and the material progressively transforms into a solid. Although the science and technology of crystal growth during solidification is relatively well understood, the prior nucleation stage has received less attention because experiments to study nucleation behavior, which takes place over short time scales and at the nano- to microscale, are difficult to perform. Notwithstanding these experimental difficulties, insightful nucleation theory has been developed from the 1950s onward (1–9), and laboratory and manufacturing experience have shown that nucleation plays a critical role in controlling the final structure and properties of many important products such as nickel alloy turbine blades and magnesium alloy automotive components. In the aluminum industry, micrometer-sized grain-refining insoluble particles are added to alloys just before casting to promote the easy nucleation of refined and isotropic aluminum-rich crystals, with beneficial effects on final mechanical properties and material consistency.

Synchrotron x-ray–based imaging techniques, such as radiography and tomography, are now used routinely to investigate the fundamentals of crystal growth in technologically important systems such as steel, Ni, Al, and other alloy systems (10–27). The latest third-generation synchrotrons have high photon energies and fluxes than can penetrate through millimeters of alloys as they are cooled from high temperature and can produce images of sufficient spatiotemporal resolution to track the two-dimensional (2D) or 3D dynamics of crystal growth. Studies of this type have been used to image equiaxed and columnar dendrites and to compare their behavior with theories of crystal shape (28–31), coarsening (29, 32–37), and morphological stability (25, 27, 38–41). However, when applying similar approaches to image directly the instant of crystal nucleation, difficulties arise due to the vanishingly small dimensions of the crystal on formation.

Here, we present a new approach to identify multiple crystal nucleation events and the temperature of crystal formation, and thus any nucleation undercooling, directly and automatically from synchrotron x-ray radiographic videos. The data are used to investigate widely used

assumptions relating to heterogeneous nucleation in alloys. Our technique relies on ensuring a well-controlled thermal field during cooling from the liquid, accurate local composition measurements, and quick detection of the crystal just after it has formed. Critically, we have trained a computer algorithm to spot new crystals automatically in video sequences and to measure their instantaneous growth rate using ideas used in computer vision (42). Once a crystal is detected by extrapolating the growth rate backward fractionally in time, the position and moment of crystal formation may be estimated, and from the measured liquid composition at this point and the relationship between composition and temperature defined by the phase diagram liquidus line, the corresponding local temperature and, hence, any undercooling at the instant of crystal formation are deduced. This approach is described in detail in the Supplementary Materials and illustrated in the Results and Discussion. Although thermal information relies on this link between local composition and temperature, other behaviors that we show, such as bursts of nucleation, are not reliant on this assumption.

In a single solidification experiment we measured up to 250 separate crystal formation events automatically from across the imaging domain and for every condition studied. We repeated identical experiments many times to give a data set of approximately 14,000 separate nucleation events. We conclude that (i) the use of efficient grain refiners led to small undercoolings of <0.5 K that were consistent with bulk measurements, (ii) the distributions of undercoolings were consistent with the widely assumed free growth model of nucleation, (iii) nucleation proceeds in repeating cycles of solute-suppressed nucleation followed by a burst of nucleation events, the strength of which relates to alloy composition through a solute-suppressed nucleation mechanism, and (iv) the machine learning and computer vision approach quickly and consistently interrogated a very large image set that was impossibly time-consuming to analyze manually.

RESULTS AND DISCUSSION

In situ imaging of solidification

Figure 1A shows the normalized crystal density as a function of time measured directly from radiographs for the Al-5Ti-1B grain-refined Al-Cu alloys with 10, 15, 20, and 25 weight % (wt %) Cu and represents the raw output of the computer vision algorithm based on typical images such as those shown in Fig. 1 (B to D). Crystal density plots are grouped into three broad shaded bands corresponding to the individual

Copyright © 2018
The Authors, some
rights reserved;
exclusive licensee
American Association
for the Advancement
of Science. No claim to
original U.S. Government
Works. Distributed
under a Creative
Commons Attribution
NonCommercial
License 4.0 (CC BY-NC).

¹Department of Materials, University of Oxford, Oxford OX1 3PH, UK. ²Department of Engineering Science, University of Oxford, Oxford OX1 3PJ, UK. ³Skolkovo Institute of Science and Technology, Moscow, Russia.

*Corresponding author. Email: enzo.liotti@materials.ox.ac.uk

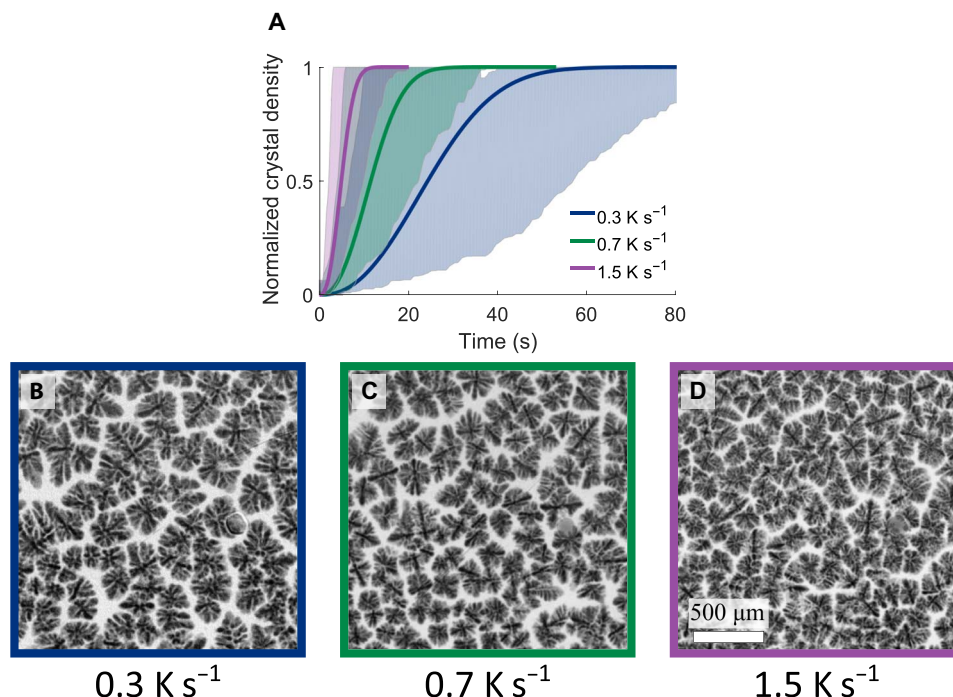


Fig. 1. Crystal density. (A) Normalized crystal density measured by the computer vision algorithm as a function of time for grained refined Al-Cu alloys with 10, 15, 20, and 25 wt % Cu, subdivided into three cooling rates of 0.3, 0.7, and 1.5 K s⁻¹ (time $t = 0$ s was set when a crystal first appeared in the field of view). The solid lines are the best-fit Avrami equation to the data. (B to D) Typical radiographic images at the three cooling rates obtained toward the end of solidification and showing the equiaxed dendritic Al-rich primary crystals in an Al-25 wt % Cu.

experiments for cooling rates of 0.3, 0.7, and 1.5 K s⁻¹ (time $t = 0$ s when the first crystal appeared in the field of view). The data set represents 13,853 separate crystal identifications by the computer vision algorithm. Figure 1A shows that the evolution of crystal number per unit volume (crystal density) was faster with increasing cooling rate. There was only comparatively weak sensitivity of normalized crystal formation rate to composition for a given cooling rate. With the fixed field of view of the experiment, the plots in Fig. 1A are essentially the fraction solid as a function of time, and assuming any changes in temperature on diffusion over the measurement period were relatively small, they may be approximated to the well-known Avrami equation (43–45) that describes the progress of a diffusion-controlled phase transformation

$$I = 1 - e^{-kt^m} \quad (1)$$

where I is the normalized density of the transformed phase (solid in this case), t is the time, and k and m are constants. The lines through the shaded regions in Fig. 1A are the plots of the best fit of Eq. 1 to the averaged and normalized crystal density as a function of time for each of the three cooling rates (that is, ignoring the weaker influence due to changes in composition). In each case, the quality of the fit was $R^2 > 0.99$ with best-fit values of $m = 2.4$, 2.5, and 2.5, respectively, which are consistent with a diffusive transformation progressing in a quasi-3D situation (44, 46) and the thin sample arrangement used. Although more sophisticated versions of Eq. 1 are available [for example, (47)], these were not explored because the primary objective of the fitting in Fig. 1A was only to ensure that the computer vision algorithm operated sensibly.

Figure 1 (B to D) displays typical radiographs of the alloys when the crystal appearance rate in the field of view has fallen to ≈ 0 , showing

equiaxed, dendritic primary Al-rich crystals filling the frame and typical of grain-refined Al alloys. Manual counting of crystals in selected images showed excellent agreement with measured crystal densities from the computer vision algorithm (see movie S1). See section S2.2.5 in the Supplementary Materials for the full validation assessment of the method.

Crystal formation rate

Differentiating the raw data in Fig. 1A before normalization gives the crystal formation rate as a function of time for the different alloy compositions at three different cooling rates and is shown in Fig. 2A. The formation rate increased initially and reached a peaked at ≈ 3 crystals s⁻¹ at 0.3 K s⁻¹ and ≈ 27 crystals s⁻¹ at 1.5 K s⁻¹; the formation rate then decreased steadily to zero. Increasing the Cu concentration increased the peak crystal formation rate only when the cooling rate was 1.5 K s⁻¹. The time period over which crystals formed increased with Cu concentration, for example, the crystal formation period at 0.3 K s⁻¹ for relatively concentrated alloys was more than 2.5 times longer than for the most dilute Al-10 wt % Cu alloy. As described later, this arose because in dilute alloy compositions, the crystals grew much larger and ongoing nucleation events were more effectively suppressed. These interdependencies are shown more clearly in the plots of crystal formation rate averaged over multiple experiments in Fig. 2 (B and C), showing again that the formation rate increased with cooling rate and was most sensitive to cooling rate at high Cu concentrations; for a given cooling rate, the crystal formation rate increased with Cu concentration.

Nucleation undercooling

Figure 3 shows a sequence of images every 0.5 s taken relatively early in the crystallization of Al-25 wt % Cu to exemplify how nucleation undercoolings were estimated. Readers are also encouraged to watch

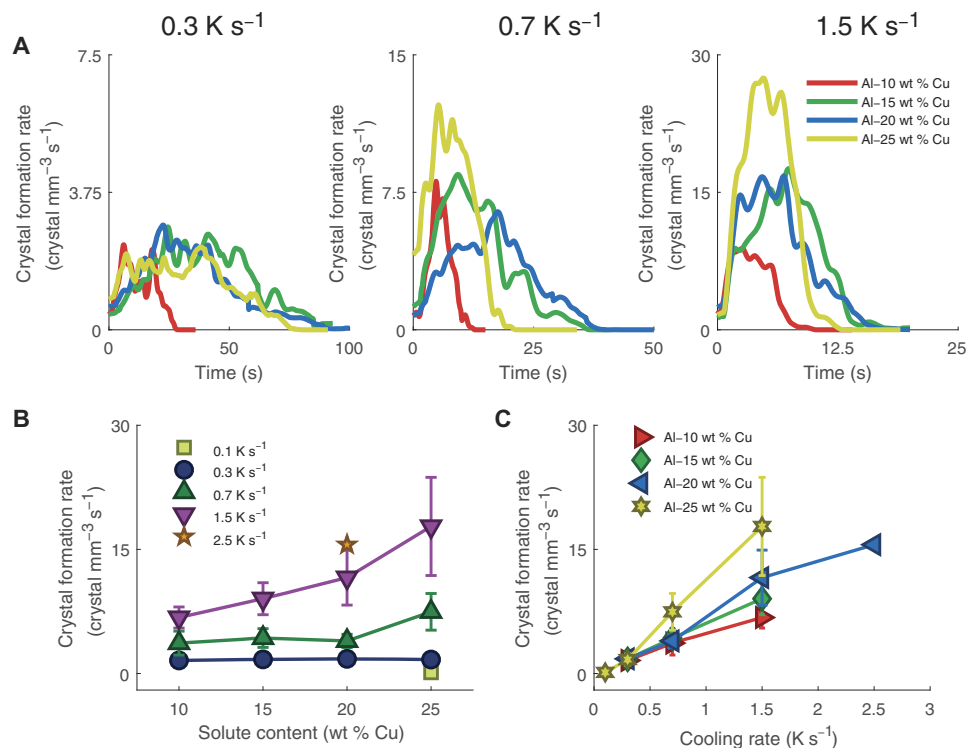


Fig. 2. Crystal formation rate. (A) Crystal formation rate as a function of time at cooling rates of 0.3, 0.7, and 1.5 K s⁻¹, and (B) as a function of solute content and (C) cooling rate.

movie S2. Crystals already identified by the computer vision algorithm in previous frames are boxed in green, whereas crystals identified for the first time in the current frame are boxed in blue. Note that the comparatively buoyant crystals moved continuously during a sequence, predominantly but not always upward, and the computer vision algorithm was able to track the movement of each crystal frame by frame, examples of which are shown in Fig. 3 by superimposed velocity vectors on each crystal, indicating crystal velocities in the range of 10 to 100 $\mu\text{m s}^{-1}$.

The second, lower sequence shows a zoom-in of five boxed-in-green crystals in the last frame of the first sequence. Subsequent images in the sequence step back in time at a higher temporal resolution of 0.15 s. Each crystal is monitored by the computer vision algorithm until it disappears, which is then assumed to be the instant and location of nucleation. As described in the Supplementary Materials, an estimate of the temperature in the box was then made according to the local Cu concentration, and by comparison with the equilibrium liquidus temperature, the undercooling was estimated.

Using this approach, Fig. 4 shows the probability density functions of the measured nucleation undercooling for each of the four alloys at each of the three cooling rates. Consistent with the known potency of the micrometer-sized TiB₂ particles in the Al-5Ti-1B grain refiner (8, 48, 49), the mean nucleation undercooling across all 12 experimental conditions was 0.2 to 0.5 K, which is in very good agreement with undercooling measurements obtained by thermocouples in grain-refined aluminum alloy melts (8, 50). For each alloy and cooling rate combination, the undercooling distributions were asymmetric and fitted closely to a log-normal distribution (dotted line), with a tail of relatively large but more infrequent undercoolings >0.5 K.

The most widely used model for heterogeneous nucleation of crystals by the action of a crystal- or grain-refining particle is termed

the free growth model (8, 51), in which the energy barrier to the nucleation of solid from liquid via the action of an efficient nucleating particle is lower for larger nucleating particles. Thus, solid crystals are formed preferentially on larger nucleating particles first at relatively low undercooling ΔT and then on progressively smaller particles at higher undercooling, according to

$$\Delta T = \frac{4\sigma}{\Delta S_v d} \quad (2)$$

where σ is the solid-liquid surface energy, ΔS_v is the entropy of fusion per unit volume, and d is the diameter of the nucleating particle. In the current experimental arrangement, it was not possible to observe the micrometer-sized nucleating TiB₂ particles directly. Nonetheless, by assuming $\sigma = 158 \text{ mJ m}^{-2}$ and $\Delta S_v = 1.112 \times 10^6 \text{ J K}^{-1} \text{ m}^{-3}$ (8), the log-normal distributions of undercooling in Fig. 4 may be translated into distributions of nucleating particle diameters using Eq. 2 and as shown in fig. S9. For example, the undercooling distribution data for Al-15 wt % Cu at 0.7 K s⁻¹ give a log-normal particle diameter distribution between 0.5 and 10 μm with a mean diameter of 2.5 μm , which is in excellent agreement with the larger particles measured in Al-5Ti-1B grain refiners (8) (noting that according to the free growth model, the nucleating particle diameter distribution will be different from the overall particle diameter distribution in the melt because only larger diameters are expected to be involved in crystal nucleation). Agreement of measured nucleation undercoolings and nucleating particle diameters with previous data supports the validity of the method to estimate undercooling based on local liquid composition. However, unlike other methods using thermocouples or pyrometers that measure average undercoolings of an ensemble of grains, here each crystallization

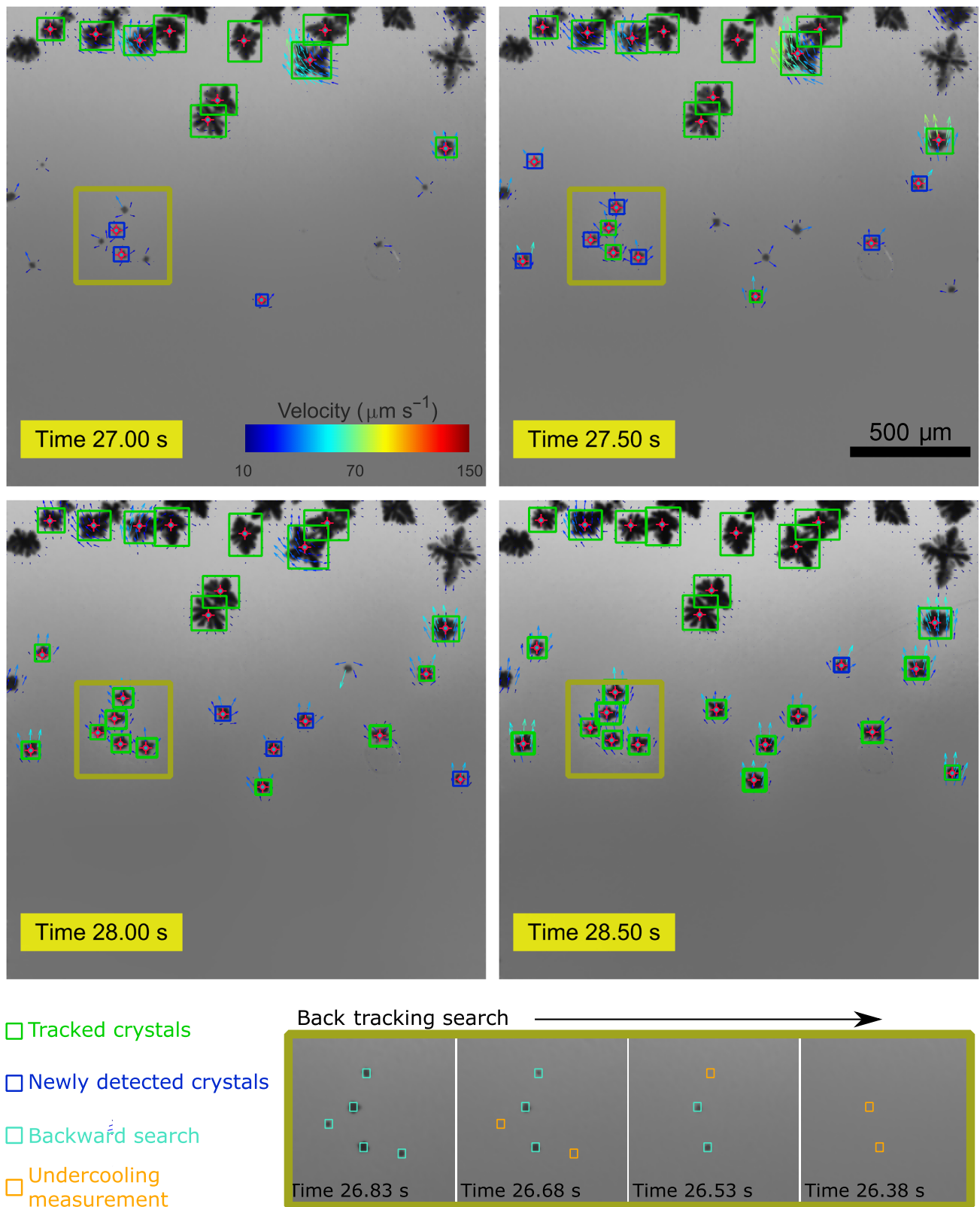


Fig. 3. Nucleation undercooling measurement method. A sequence of images of 1.5 s from the crystallization of an Al-25 wt % Cu alloy: Previously identified crystals are boxed in green, and crystals identified for the first time in each frame are boxed in blue. A cluster of five crystals are boxed in yellow and shown at higher magnification in the second sequence, which is in reverse time. The five grains are tracked with reverse time back through the sequence at higher temporal resolution (0.15 s) until each disappears, which is then assumed to be the instant and location of nucleation from which an estimate of undercooling is made according to the local Cu composition.

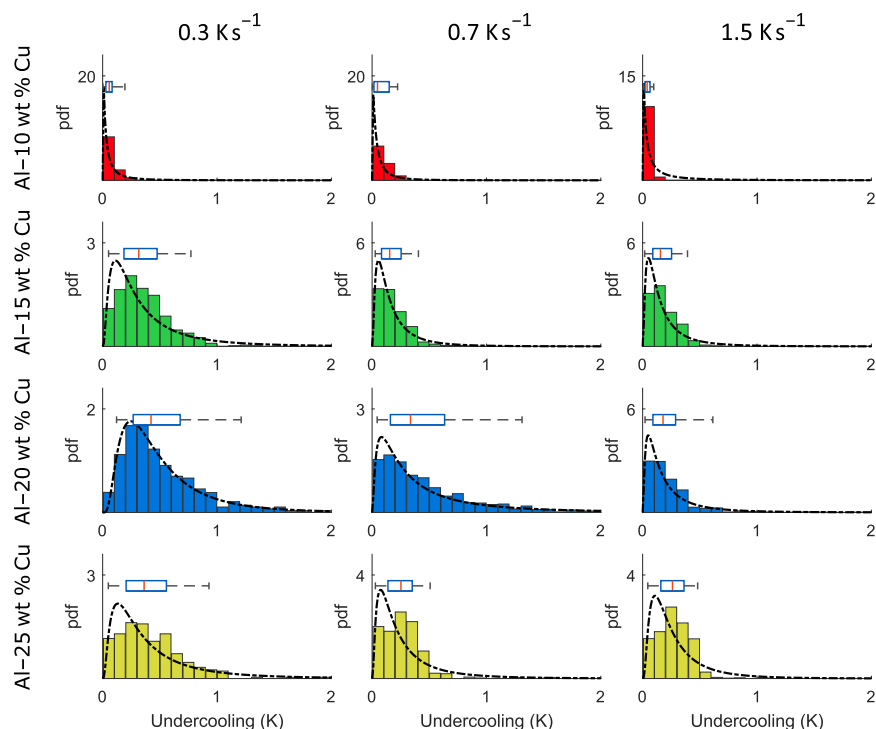


Fig. 4. Nucleation undercooling distributions. The undercooling probability density function (pdf) distributions for each of the 12 experimental conditions. Each one comprises several repeat experiments, together with a best-fit log-normal distribution (dotted line) and a box-plot insert showing the position of the median undercooling (red line), the second and third quartiles (blue box), and the 5 to 95 percentiles. The bin width is 0.01 wt % Cu. The data set includes 6200 validated measurements.

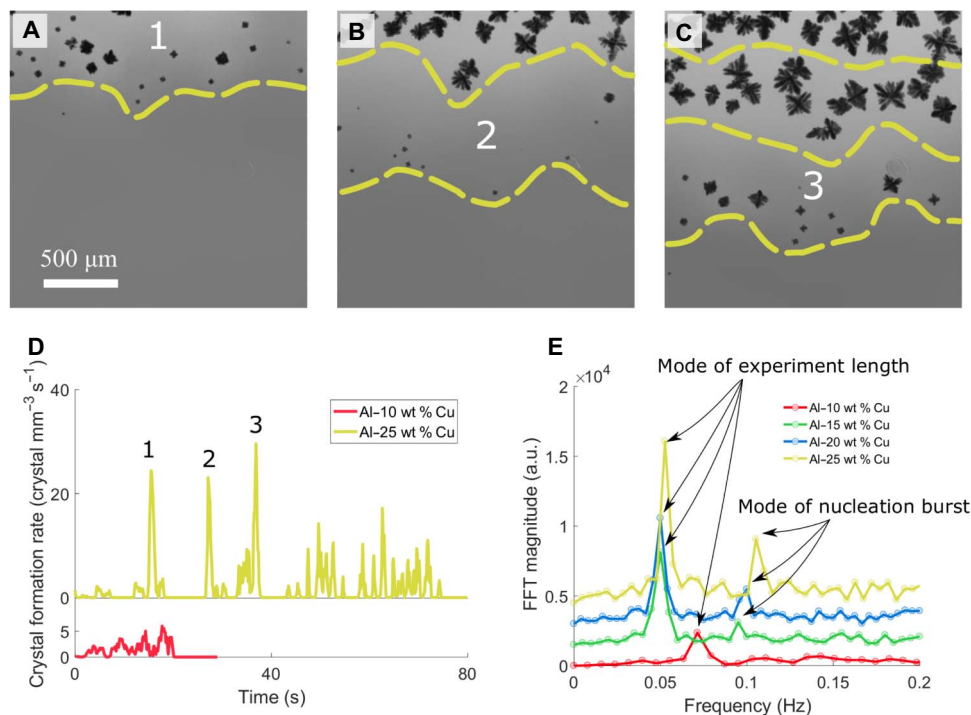


Fig. 5. Nucleation bursts. (A to C) Solidification of an Al-25 wt % Cu grain-refined with 0.1 wt % Ti using Al-5Ti-1B and cooled at a constant rate of 0.3 K s^{-1} ; image frames at time $t = 16, 29$, and 38 s showing, respectively, three successive nucleation waves (time $t = 0 \text{ s}$ was set to the first frame in which a crystal appeared; the colormap is an inverted gray scale to enhance crystal visibility). (D) The crystal formation rate as a function of time of the experiment shown in (A) to (C) (yellow line) showing more pronounced bursts of nucleation as the alloy composition increased (at 0.3 K s^{-1}). (E) The frequency spectrum of the crystal formation rate as a function of time for the four Al-Cu alloys at 1.5 K s^{-1} . a.u., arbitrary units; FFT, fast Fourier transform.

event was resolved individually so that an undercooling distribution was obtained in a single experiment for each crystallization condition.

Figure 4 shows that the mean and spread of measured undercoolings were relatively insensitive to cooling rate because of the efficiency of the TiB₂ nucleating particles—this is their function in commercial practice—although, in general, the mean and spread of undercoolings decreased with increasing cooling rate. It was marked also that the spread of undercoolings became broader with increasing alloy composition, which is discussed further below.

Solute-suppressed nucleation

Figure 5 (A to C) shows images of the solidification of grain-refined Al–25 wt % Cu cooled at a constant rate of 0.3 K s^{−1}, showing behavior representative of all experiments. Readers are encouraged to watch movie S3. Equiaxed dendritic crystals started to form at the top of the field of view with crystals then appearing progressively along the direction of the (inevitable) small thermal gradient (estimated at <1 K mm^{−1}). Crystals appeared in bursts ahead of the front of existing grains (shown by the dotted yellow line), in bands labeled 1 to 3 across the frame. The corresponding crystal formation rate as a function of time is shown in Fig. 5D, confirming that crystals appeared in distinct bursts; similar data are also shown for Al–10 wt % Cu with much less distinct nucleation bursts.

Albeit with different intensities, these nucleation bursts were evident in all experiments and were investigated further using a frequency domain Fourier analysis in MATLAB software for each experimental condition. For illustrative purposes, Fig. 5E shows typical resulting frequency plots for all alloy compositions, in this case at a cooling rate of 1.5 K s^{−1}. The first (strongest) peak (or mode) indicated the typical time period (inverse of mode frequency) of the experiment itself: Experiments for Al–10 wt % Cu were comparatively short at 0.07 Hz and ≈14 s because few grains formed and counting automatically stopped relatively quickly; for Al–25 wt % Cu, there were more grains in total, and experiments continued for longer at 0.05 Hz and ≈20 s. The second strongest mode relates to the characteristic frequency of crystal appearance. This mode was more easily resolved when alloy composition increased because there were more crystals at higher composition and the signal-to-noise ratio was improved. As alloy composition increased, the bursts were also more distinct (larger relative amplitude in the frequency plots in Fig. 5E) with a frequency of ≈0.1 Hz and broadly consistent with the time series data in Fig. 5D. This trend was reproduced across all experiments as summarized in fig. S10 and table S2. Thus, taking into account the undercooling distributions already shown in Fig. 4, nucleation behavior may be summarized as follows: At low alloy concentration, nucleation tended to be at low undercooling and crystal appearance was close to continuous; at higher alloy concentrations, the range of nucleation undercoolings increased and proceeded with more distinct bursts of crystal appearance with a characteristic frequency. Qualitative observations of bursts of nucleation (in the presence of a thermal gradient) have also been reported in the studies by Prasad *et al.* (52, 53).

Returning to the radiographs in Fig. 5 (A to C), it was readily observed—most notably for Al–25 wt % Cu that had the largest number of crystals—that there was a solute-enriched region ahead and/or around newly formed crystals in which the subsequent appearance of a new crystal was comparatively rare. It has been theorized that this type of solute enrichment leads to a solute-suppressed nucleation zone (SSNZ) around/ahead of crystals. For an alloy with an equilibrium partition coefficient $k < 1$ (such as $k = 0.17$ for the Al–Cu alloys

here), an SSNZ forms because solute rejected into undercooled liquid by a solid crystal as it grows enriches the liquid near the solid-liquid interface so that its equilibrium freezing temperature (that is, the alloy liquidus temperature) is higher than the actual temperature of the undercooled liquid (see the schematic sequences in fig. S11). Thus, the thermodynamic driving force for nucleation is eliminated in the SSNZ and nucleation is “suppressed.”

It was initially conjectured that the variations in undercooling and nucleation behavior with cooling rate and composition shown in Fig. 4 were due to changes in the width of the SSNZ. However, although both extensive automated and manual measurements were performed on all data to estimate the SSNZ under different assumptions (for example, distance to nearest crystal neighbor, width of solute-enriched zone), no meaningful link could be established between SSNZ width and any aspect of the undercooling or nucleation data. The average SSNZ width varied little from experiment to experiment, and the spread of widths within a particular experiment was always in the range of 50 to 100 μm, depending on which particular assumption for its definition was used. Instead, it was the fraction of solute-enriched liquid that linked undercooling and nucleation behavior, as described below.

Figure 6A shows a pair of radiographs during the solidification of Al–10 wt % Cu and Al–25 wt % Cu at a solid fraction of 0.02 and 0.03, respectively. In each of the radiographs, the solid crystals are shown in black, liquid of the alloy composition $C_0 = 10$ or 25 wt % Cu is shown in green, and any liquid with a Cu concentration greater than $C_0 + 0.03$ wt % (solute-enriched) is shown in blue. Note that for each image pair, the solid fraction is constant and that horizontal bands of new crystals are more pronounced at the higher concentration. Because the solute-enriched zone around a grain did not vary strongly with concentration, a consequence of there being more crystals in the more concentrated alloys is that the fraction of the remaining liquid that was solute-rich (f_E) increased: rising from 0.33 to 0.57 as concentration increased from 10 to 25 wt % Cu at a solid fraction of 0.02 and from 0.38 to 0.69 for the same alloys at a solid fraction of 0.03. The impact of this increasing fraction of solute-rich liquid on nucleation behavior is shown schematically in Fig. 6B. The upper graphs show the distribution of the randomly distributed potential TiB₂ nucleants in the melt along with the resulting distribution of measured nucleation undercoolings before any significant crystal formation or solute-enriched liquid. As already described, the nucleation events take place preferentially on the larger-diameter (red) but comparatively rare nucleants. In the lower graphs, after some crystals have been formed due to the efficient action of the relatively large but rare nucleants, a fraction of the liquid has become solute-rich, and a proportion of the remaining potential nucleants—including some of the most efficient—are rendered inactive. As heat continues to be removed, the subsequent burst of nucleation will, on average, tend to be catalyzed by slightly smaller, less-efficient but more populous nucleants. As nucleation proceeds the fraction of remaining liquid in the field of view experiencing SSNZ will increase, and there will be a progressive suppression of the rarer, efficient nucleants and a shift to nucleation by more populous but more inefficient smaller-diameter nucleants. Solute suppression of efficient nucleants leads to a temporal pause in recorded nucleation events while additional heat is extracted to activate the smaller, less-efficient nucleants. Spatially, this appears as a band of no nucleation in the radiographs due to the slight but unavoidable temperature gradient. Because the smaller-diameter, now active, nucleants are more populous, subsequent nucleation events appear as distinct bursts in the time domain (or characteristic frequency) and as a wave in the spatial domain. Over

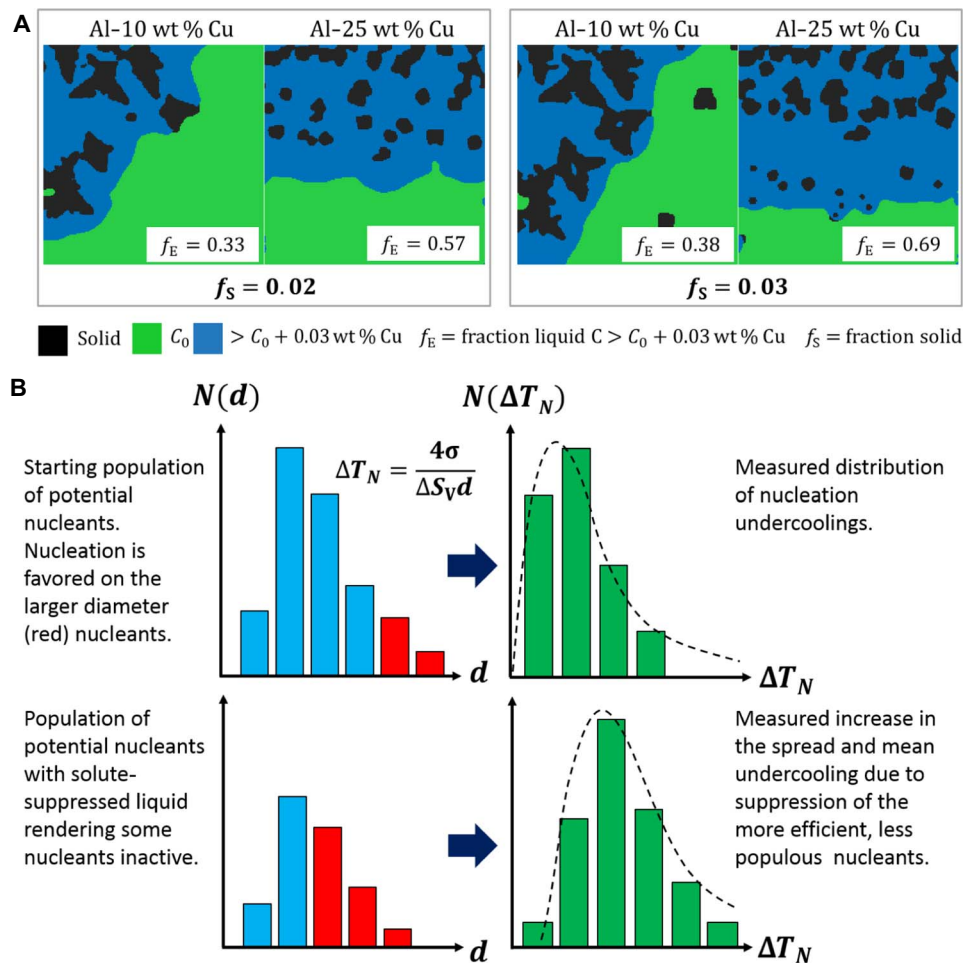


Fig. 6. Solute-suppressed nucleation. (A) Fraction of the solute-enriched liquid (f_E in blue) at fraction solid f_S of 0.02 and 0.03 during the solidification of Al-10 wt % Cu and Al-25 wt % Cu. (B) Schematic representation of the size distribution of the nucleant particles and corresponding measured nucleation undercooling without (top) and with (bottom) solute suppression of nucleation.

repeating cycles of nucleation bursts in an experiment, the overall effect on measured nucleation undercooling distribution is a broadening of the distribution and a shift to higher mean undercoolings, as shown in Fig. 4.

The key insights over previous work are the following:

1) A large data set to evidence that nucleation occurs in bursts, the strength of which relates to the probability of potent nucleants being solute-suppressed.

2) In a fixed field of view, the extent of solute suppression in the remaining liquid as a whole (not simply around a single crystal) determines the statistical distribution of nucleation undercoolings.

3) Nucleation under conditions where a high fraction of the remaining liquid is enriched tends to promote higher undercoolings because less-efficient nucleants become active, and because these nucleants are more populous, a higher total number of crystals per unit volume are produced once integrated over an ensemble of nucleation events.

The crystal size data as a function of composition here are consistent with many reports, based on metallographic analysis of laboratory castings, that describe smaller crystal (or grain) sizes with increasing alloy solute content (8, 54, 55). We suggest that reduced final crystal sizes with increasing composition arise through a two-step process: Solute sup-

pression of “easy” nucleation at low undercooling (in probabilistic terms) that then promotes delayed, more “difficult” nucleation at a higher undercooling, which overall is more efficient in generating new crystals.

CONCLUSIONS

A computer vision algorithm was trained using a machine learning approach to recognize crystals forming in slowly cooled, grain-refined Al-Cu alloys, allowing quantified information to be extracted from terabytes of otherwise unanalyzable x-ray radiographic videos. The approach allowed the crystal formation rate, crystal growth rate, and crystal movement to be quantified for each crystal as a function of time. On the basis of local composition measurements from the images, nucleation undercoolings for each crystal formation event were estimated. The data showed very good agreement with widely used theory such as Avrami kinetics and the free growth model of nucleation, and, where preexisting data were available, also showed good quantitative agreement of nucleation undercoolings. Increasing the fraction liquid experiencing solute suppression during alloy nucleation and equiaxed crystal growth was shown to promote discontinuous bursts of nucleation at comparatively higher nucleation undercoolings that increased the efficiency of crystal formation.

MATERIALS AND METHODS

Experiments were performed on the ID19 beamline at the European Synchrotron Radiation Facility (ESRF) using a bespoke solidification rig specifically designed to work in the synchrotron environment. Full details of the experimental setup can be found in the Supplementary Materials and in our previous publications (25, 27). Thin foil samples were solidified in a near-isothermal condition, cooling from the fully liquid state at a constant rate. Four Al-Cu alloy compositions were investigated containing 10, 15, 20, and 25 wt % Cu. An Al-5Ti-1B grain refiner, containing a large number of micrometer-sized TiB₂ particles, was added to all alloys at 0.1 wt % Ti concentration to promote nucleation and to ensure equiaxed rather than extended columnar crystals. For each alloy, cooling rates of 0.3, 0.7, and 1.5 K s⁻¹ were studied, along with a smaller number of experiments at 0.1 and 2.5 K s⁻¹. As shown in table S1, 128 videos were recorded that included several repeats of each condition. The videos were automatically analyzed using a machine learning-based algorithm, which we have developed (described in detail in the Supplementary Materials).

SUPPLEMENTARY MATERIALS

Supplementary material for this article is available at <http://advances.sciencemag.org/cgi/content/full/4/4/eaar4004/DC1>

section S1. Synchrotron experiments

section S2. Automatic analysis of radiographic sequences

section S3. Supplementary results

fig. S1. Sample preparation steps.

fig. S2. Experimental setup.

fig. S3. Image processing steps to obtain an intensity image and solute map.

fig. S4. Density map overview.

fig. S5. Variation in crystal size and density for three different sequences.

fig. S6. Localizing crystals through the density map.

fig. S7. Counting accuracy.

fig. S8. Undercooling measurement.

fig. S9. Nucleant particle diameters.

fig. S10. Nucleation burst frequencies analysis.

fig. S11. Solute suppression mechanism.

table S1. Sample summary.

table S2. Nucleation burst frequencies.

movie S1. Comparison between manual and automatic crystal counting.

movie S2. Crystal detection and tracking.

movie S3. Crystal formation rate and nucleation bursts.

References (56–71)

REFERENCES AND NOTES

1. J. C. Fisher, J. H. Hollomon, D. Turnbull, Nucleation. *J. Appl. Phys.* **19**, 775–784 (1948).
2. D. Turnbull, J. C. Fisher, Rate of nucleation in condensed systems. *J. Chem. Phys.* **17**, 71–73 (1949).
3. D. Turnbull, Kinetics of heterogeneous nucleation. *J. Chem. Phys.* **18**, 198–203 (1950).
4. D. Turnbull, Theory of catalysis of nucleation by surface patches. *Acta Metall.* **1**, 8–14 (1953).
5. J. H. Hollomon, D. Turnbull, Nucleation. *Prog. Met. Phys.* **4**, 333–388 (1953).
6. I. Maxwell, A. Hellawell, A simple model for grain refinement during solidification. *Acta Metall.* **23**, 229–237 (1975).
7. B. Cantor, R. D. Doherty, Heterogeneous nucleation in solidifying alloys. *Acta Metall.* **27**, 33–46 (1979).
8. A. L. Greer, A. M. Bunn, A. Tronche, P. V. Evans, D. J. Bristow, Modelling of inoculation of metallic melts: Application to grain refinement of aluminium by Al-Ti-B. *Acta Mater.* **48**, 2823–2835 (2000).
9. D. H. StJohn, M. Qian, M. A. Easton, P. Cao, The interdependence theory: The relationship between grain formation and nucleant selection. *Acta Mater.* **59**, 4907–4921 (2011).
10. H. Yasuda, T. Nagira, M. Yoshiya, N. Nakatsuka, A. Sugiyama, K. Uesugi, K. Umetani, Development of x-ray imaging for observing solidification of carbon steels. *ISIJ Int.* **51**, 402–408 (2011).
11. T. Nagira, C. M. Gourlay, A. Sugiyama, M. Uesugi, Y. Kanzawa, M. Yoshiya, K. Uesugi, K. Umetani, H. Yasuda, Direct observation of deformation in semi-solid carbon steel. *Scr. Mater.* **64**, 1129–1132 (2011).
12. M. A. Azeem, P. D. Lee, A. B. Phillion, S. Karagadde, P. Rockett, R. C. Atwood, L. Courtois, K. M. Rahman, D. Dye, Revealing dendritic pattern formation in Ni, Fe and Co alloys using synchrotron tomography. *Acta Mater.* **128**, 241–248 (2017).
13. R. H. Mathiesen, L. Arnberg, F. Mo, T. Weitkamp, A. Snigirev, Time resolved x-ray imaging of dendritic growth in binary alloys. *Phys. Rev. Lett.* **83**, 5062–5065 (1999).
14. R. H. Mathiesen, L. Arnberg, K. Ramsøskar, T. Weitkamp, C. Rau, A. Snigirev, Time-resolved x-ray imaging of aluminum alloy solidification processes. *Metall. Mater. Trans. B* **33**, 613–623 (2002).
15. D. Ruvalcaba, R. H. Mathiesen, D. G. Eskin, L. Arnberg, L. Katgerman, In situ observations of dendritic fragmentation due to local solute-enrichment during directional solidification of an aluminum alloy. *Acta Mater.* **55**, 4287–4292 (2007).
16. R. H. Mathiesen, L. Arnberg, X-ray radiography observations of columnar dendritic growth and constitutional undercooling in an Al–30wt%Cu alloy. *Acta Mater.* **53**, 947–956 (2005).
17. R. H. Mathiesen, L. Arnberg, H. Nguyen-Thi, B. Billia, In situ x-ray video microscopy as a tool in solidification science. *JOM* **64**, 76–82 (2012).
18. K. V. Falch, D. Casari, M. Di Michiel, C. Detlefs, A. Snigireva, I. Snigireva, V. Honkimäki, R. H. Mathiesen, In situ hard x-ray transmission microscopy for material science. *J. Mater. Sci.* **52**, 3497–3507 (2017).
19. D. Casari, W. U. Mirihanage, K. V. Falch, I. G. Ringdalen, J. Friis, R. Schmid-Fetzer, D. Zhao, Y. Li, W. H. Sillekens, R. H. Mathiesen, α -Mg primary phase formation and dendritic morphology transition in solidification of a Mg-Nd-Gd-Zn-Zr casting alloy. *Acta Mater.* **116**, 177–187 (2016).
20. A. Buffet, G. Reinhart, T. Schenk, H. Nguyen-Thi, J. Gastaldi, N. Mangelinck-Noël, H. Jung, J. Härtwig, J. Baruchel, B. Billia, Real-time and in situ solidification of Al-based alloys investigated by synchrotron radiation: A unique experimental set-up combining radiography and topography techniques. *Phys. Stat. Sol.* **204**, 2721–2727 (2007).
21. B. Billia, N. Bergeon, H. Nguyen-Thi, H. Jamgotchian, J. Gastaldi, G. Grange, Cumulative mechanical moments and microstructure deformation induced by growth shape in columnar solidification. *Phys. Rev. Lett.* **93**, 126105 (2004).
22. H. Nguyen-Thi, L. Salvo, R. H. Mathiesen, L. Arnberg, B. Billia, M. Suéry, G. Reinhart, On the interest of synchrotron x-ray imaging for the study of solidification in metallic alloys. *C. R. Phys.* **13**, 237–245 (2012).
23. C. Puncrebut, A. B. Phillion, J. L. Fife, P. D. Lee, Coupling in situ synchrotron x-ray tomographic microscopy and numerical simulation to quantify the influence of intermetallic formation on permeability in aluminium–silicon–copper alloys. *Acta Mater.* **64**, 316–325 (2014).
24. E. Liotti, A. Lui, R. Vincent, S. Kumar, Z. Guo, T. Connolley, M. Hart, L. Arnberg, R. H. Mathiesen, P. S. Grant, A synchrotron x-ray radiography investigation of induced dendrite fragmentation in Al-15wt%Cu. *Mater. Sci. Forum* **765**, 210–214 (2013).
25. E. Liotti, A. Lui, R. Vincent, S. Kumar, Z. Guo, T. Connolley, I. P. Dolbnya, M. Hart, L. Arnberg, R. H. Mathiesen, P. S. Grant, A synchrotron x-ray radiography study of dendrite fragmentation induced by a pulsed electromagnetic field in an Al-15Cu alloy. *Acta Mater.* **70**, 228–239 (2014).
26. E. Liotti, A. Lui, T. Connolley, I. P. Dolbnya, K. J. S. Sawhney, A. Malandain, M. D. Wilson, M. C. Veale, P. Seller, P. S. Grant, Mapping of multi-elements during melting and solidification using synchrotron x-rays and pixel-based spectroscopy. *Sci. Rep.* **5**, 15988 (2015).
27. E. Liotti, A. Lui, S. Kumar, Z. Guo, C. Bi, T. Connolley, P. S. Grant, The spatial and temporal distribution of dendrite fragmentation in solidifying Al-Cu alloys under different conditions. *Acta Mater.* **121**, 384–395 (2016).
28. N. Limodin, L. Salvo, E. Boller, M. Suéry, M. Felberbaum, S. Gaillière, K. Madi, In situ and real-time 3-D microtomography investigation of dendritic solidification in an Al-10 wt.% Cu alloy. *Acta Mater.* **57**, 2300–2310 (2009).
29. D. Tolnai, P. Townsend, G. Requena, L. Salvo, J. Lendvai, H. P. Degischer, In situ synchrotron tomographic investigation of the solidification of an AlMg4.7Si8 alloy. *Acta Mater.* **60**, 2568–2577 (2012).
30. A. Bogno, H. Nguyen-Thi, A. Buffet, G. Reinhart, B. Billia, N. Mangelinck-Noël, N. Bergeon, J. Baruchel, T. Schenk, Analysis by synchrotron x-ray radiography of convection effects on the dynamic evolution of the solid–liquid interface and on solute distribution during the initial transient of solidification. *Acta Mater.* **59**, 4356–4365 (2011).
31. S. Shuai, E. Guo, A. B. Phillion, M. D. Callaghan, T. Jing, P. D. Lee, Fast synchrotron x-ray tomographic quantification of dendrite evolution during the solidification of Mg–Sn alloys. *Acta Mater.* **118**, 260–269 (2016).
32. B. Li, H. D. Brody, A. Kazimirov, Real-time observation of dendrite coarsening in Sn-13%Bi alloy by synchrotron microradiography. *Phys. Rev. E* **70**, 062602 (2004).

33. N. Limodin, L. Salvo, M. Suéry, M. DiMichiel, In situ investigation by x-ray tomography of the overall and local microstructural changes occurring during partial remelting of an Al–15.8 wt.% Cu alloy. *Acta Mater.* **55**, 3177–3191 (2007).
34. S. Terzi, L. Salvo, M. Suery, A. K. Dahle, Coarsening mechanisms during isothermal holding of a dendritic Al–10wt%Cu alloy. *Trans. Indian Inst. Met.* **62**, 447–449 (2009).
35. D. Ruvalcaba, R. H. Mathiesen, D. G. Eskin, L. Arnberg, L. Katgerman, In-situ analysis of coarsening during directional solidification experiments in high-solute aluminum alloys. *Metall. Mater. Trans. B* **40**, 312–316 (2009).
36. L. K. Aagesen, A. E. Johnson, J. L. Fife, P. W. Voorhees, M. J. Miksis, S. O. Poulsen, E. M. Lauridsen, F. Marone, M. Stampanoni, Pinch-off of rods by bulk diffusion. *Acta Mater.* **59**, 4922–4932 (2011).
37. J. L. Fife, J. W. Gibbs, E. B. Gulsoy, C.-L. Park, K. Thornton, P. W. Voorhees, The dynamics of interfaces during coarsening in solid–liquid systems. *Acta Mater.* **70**, 66–78 (2014).
38. G. Reinhart, A. Mangelinck-Noël, H. Nguyen-Thi, T. Schenk, J. Gastaldi, B. Billia, P. Pino, J. Hartwig, J. Baruchel, Investigation of columnar–equiaxed transition and equiaxed growth of aluminium based alloys by x-ray radiography. *Mater. Sci. Eng. A* **413**, 384–388 (2005).
39. R. H. Mathiesen, L. Arnberg, P. Bleuet, A. Somogyi, Crystal fragmentation and columnar-to-equiaxed transitions in Al–Cu studied by synchrotron x-ray video microscopy. *Metall. Mater. Trans. A* **37**, 2515–2524 (2006).
40. H. Nguyen-Thi, G. Reinhart, N. Mangelinck-Noël, H. Jung, B. Billia, T. Schenk, J. Gastaldi, J. Härtwig, J. Baruchel, In-situ and real-time investigation of columnar-to-equiaxed transition in metallic alloy. *Metall. Mater. Trans. A* **38**, 1458–1464 (2007).
41. H. Jung, N. Mangelinck-Noël, H. Nguyen-Thi, B. Billia, Columnar to equiaxed transition during directional solidification in refined Al-based alloys. *J. Alloys Compd.* **484**, 739–746 (2009).
42. C. Arteta, V. Lempitsky, J. A. Noble, A. Zisserman, Interactive object counting, in *Proceedings of the European Conference on Computer Vision* (Springer, 2014), pp. 504–518.
43. M. Avrami, Kinetics of phase change. I general theory. *J. Chem. Phys.* **7**, 1103–1112 (1939).
44. M. Avrami, Kinetics of phase change. II transformation-time relations for random distribution of nuclei. *J. Chem. Phys.* **8**, 212–224 (1940).
45. M. Avrami, Kinetics of phase change III: Granulation, phase change, and microstructure. *J. Chem. Phys.* **9**, 177–184 (1941).
46. D. V. Louzguine-luzgin, G. Xie, A. Inoue, Nanocrystallization in Al-based metallic glasses, in *Proceedings of the 12th International Conference on Aluminium Alloys* (2010), pp. 799–804.
47. J. W. Christian, *The Theory of Transformations in Metals and Alloys, Part I and II* (Elsevier, ed. 3, 2002).
48. A. L. Greer, P. S. Cooper, M. W. Meredith, W. Schneider, P. Schumacher, J. A. Spittle, A. Tronche Grain refinement of aluminium alloys by inoculation. *Adv. Eng. Mater.* **5**, 81–91 (2003).
49. T. E. Quested, Understanding mechanisms of grain refinement of aluminium alloys by inoculation. *Mater. Sci. Technol.* **20**, 1357–1369 (2004).
50. T. E. Quested, A. L. Greer, The effect of the size distribution of inoculant particles on as-cast grain size in aluminium alloys. *Acta Mater.* **52**, 3859–3868 (2004).
51. A. L. Greer, Overview: Application of heterogeneous nucleation in grain-refining of metals. *J. Chem. Phys.* **145**, 211704 (2016).
52. A. Prasad, S. D. McDonald, H. Yasuda, K. Nogita and D. H. StJohn, A real-time synchrotron x-ray study of primary phase nucleation and formation in hypoeutectic Al–Si alloys. *J. Cryst. Growth* **430**, 122–137 (2015).
53. A. Prasad, E. Liotti, S. D. McDonald, K. Nogita, H. Yasuda, P. S. Grant, D. H. StJohn, Real-time synchrotron x-ray observations of equiaxed solidification of aluminium alloys and implications for modelling. *IOP Conf. Ser.: Mater. Sci. Eng.* **84**, 012014 (2015).
54. J. A. Spittle, S. Sadli, Effect of alloy variables on grain refinement of binary aluminium alloys with Al–Ti–B. *Mater. Sci. Technol.* **11**, 533–537 (1995).
55. M. Easton, D. H. StJohn, An analysis of the relationship between grain size, solute content, and the potency and number density of nucleant particles. *Metall. Mater. Trans. A Phys. Metall. Mater. Sci.* **36**, 1911–1920 (2005).
56. C. Tomasi, R. Manduchi, Bilateral filtering for gray and color images, in *Proceedings of the Sixth International Conference on Computer Vision* (IEEE, 1998), pp. 839–846.
57. J. Zhang, S. Ma, M. Sameki, S. Sclaroff, M. Betke, Z. Lin, X. Shen, B. Price, R. Mëch. Salient object subitizing, in *IEEE Conference on Computer Vision and Pattern Recognition* (IEEE, 2015), pp. 4045–4054.
58. T. N. Mundhenk, G. Konjevod, W. A. Sakla, K. Boakye, A large contextual dataset for classification, detection and counting of cars with deep learning, *European Conference on Computer Vision* (Springer, 2016), pp.785–800.
59. P. Chattopadhyay, R. Vedantam, R. R. Selvaraju, D. Batra and D. Parikh, Counting everyday objects in everyday scenes. arXiv:1604.03505 (2016).
60. V. Lempitsky, A. Zisserman, Learning to count objects in images, in *Advances in Neural Information Processing Systems* (2010), pp. 1324–1332.
61. L. Fiaschi, U. Köethe, R. Nair, F. A. Hamprecht, Learning to count with regression forest and structured labels, in *Proceedings of the 2012 21st International Conference on Pattern Recognition* (IEEE, 2012), pp. 2685–2688.
62. C. Arteta, V. Lempitsky, A. Zisserman, Counting in the wild, in *Proceedings of the European Conference on Computer Vision* (Springer, 2016), pp. 483–498.
63. W. Xie, J. A. Noble and A. Zisserman, Microscopy cell counting and detection with fully convolutional regression networks. *Comput. Methods Biomech. Biomed. Eng. Imaging Vis.* **2016**, 1–10 (2016).
64. M. Varma, A. Zisserman, Texture classification: Are filter banks necessary? in *Proceedings of the 2003 IEEE Computer Society Conference on Computer Vision and Pattern Recognition* (IEEE, 2003), pp. II–691.
65. F. Perronnin, Y. Liu, J. Sánchez, H. Poirier, Large-scale image retrieval with compressed fisher vectors, in *Proceedings of the 2010 IEEE Conference on Computer Vision and Pattern Recognition* (IEEE, 2010), pp. 3384–3391.
66. J. Matas, O. Chum, M. Urban, T. Pajdla, Robust wide-baseline stereo from maximally stable extremal regions. *Image Vis. Comput.* **22**, 761–767 (2004).
67. A. Vedaldi, B. Fulkerson, VLFeat: An open and portable library of computer vision algorithms, in *Proceedings of the 18th ACM International Conference on Multimedia* (ACM, 2008), pp. 1469–1472.
68. G. Farnebäck, Two-frame motion estimation based on polynomial expansion, in *Image Analysis. SCIA 2003*, J. Bigun, T. Gustavsson, Eds. (Springer, 2003), 363–370 pp.
69. J. L. Murray, The aluminium-copper system. *Int. Metals Rev.* **30**, 211–234 (1985).
70. W. Kurz, D. J. Fisher, *Fundamentals of Solidification* (Trans Tech Publications, ed. 4, 1998).
71. W. U. Mirihanage, K. V. Falch, I. Snigireva, Y. J. Li, L. Arnberg, R. H. Mathiesen, Retrieval of three-dimensional spatial information from fast in situ two-dimensional synchrotron radiography of solidification microstructure evolution. *Acta Mater.* **81**, 241–247 (2014).

Acknowledgments: We thank Luis Saucedo-Mora (Oxford) for the help during beamtime, and Alexander Rack (ESRF) for the optimization of the beamline setup for solute measurement and the extensive support received during the experiment. **Funding:** We thank the UK Engineering and Physical Sciences Research Council for funding through the Future Manufacturing Hub in Liquid Metal Engineering (EP/N007638/1) and Programme Grant Seebibyte: Visual Search for the Era of Big Data (EP/M013774/1). This work was enabled by synchrotron beamtime at ESRF ID19 (experiment no. MA2035). **Author contributions:** E.L. and P.S.G. conceived and prepared the beamtime proposal. E.L. designed the experiment. E.L. and A.L. prepared the experimental setup and conducted the experiments. C.A., V.L., and A.Z. developed the automatic machine learning algorithm. E.L. developed the algorithm to extract solidification measurements. E.L. and P.S.G. carried out the data analysis and drafted the manuscript. All the authors read and approved the manuscript. **Competing Interests:** The authors declare that they have no competing interests. **Data and materials availability:** All data needed to evaluate the conclusions in the paper are present in the paper and/or the Supplementary Materials. Additional data related to this paper may be requested from the authors.

Submitted 3 November 2017

Accepted 22 February 2018

Published 13 April 2018

10.1126/sciadv.aar4004

Citation: E. Liotti, C. Arteta, A. Zisserman, A. Lui, V. Lempitsky, P. S. Grant, Crystal nucleation in metallic alloys using x-ray radiography and machine learning. *Sci. Adv.* **4**, eaar4004 (2018).